Research Square

Preprints are preliminary reports that have not undergone peer review.
They should not be considered conclusive, used to inform clinical practice,
or referenced by the media as validated information.

Silane modified hemp shives and cellulose nanocrystals improve the strength and thermal insulation of alkali activated fly ash composites

Devesh Ojha

dojha@lko.amity.edu

Amity University

Bandana Ojha

Amity University

Research Article

Keywords: alkali-activated fly ash, hempcrete, cellulose nanocrystals, silane treatment, thermal conductivity, embodied carbon

Posted Date: November 10th, 2026

DOI: https://doi.org/10.21203/rs.3.rs-11389069/v1

License: This work is licensed under a Creative Commons Attribution 4.0 International License.
Read Full License

Additional Declarations: No competing interests reported.

Silane modified hemp shives and cellulose nanocrystals improve the strength and thermal insulation of alkali activated fly ash composites

Devesh Ojha[a,*], Bandana Ojha[b]

[a] *Department of Civil Engineering, Amity University, Lucknow, India*

[b] *Department of Computer Science & Engineering, Amity University, Ranchi, India*

[*] Corresponding author: Devesh Ojha, dojha@lko.amity.edu; ORCID: 0000-0003-2814-9555

Abstract

Hempcrete combines low thermal conductivity with biogenic carbon storage, but its compressive strength is typically 1 MPa or lower, whereas alkali-activated fly ash binders are strong but dense and carry an activator-related carbon burden. This study develops an alkali-activated fly ash–hemp–nanocellulose composite (AAFHN) in which hemp shives are alkali-washed and modified with 3-aminopropyltriethoxysilane (APTES), and cellulose nanocrystals (CNC) are dispersed in the activator solution. Five mixes were compared: an OPC control, a hemp–lime reference and three fly ash–hemp mixes with 0, 0.50 and 0.75 wt% CNC (relative to fly ash). The best-performing mix (M4; bulk density 780 kg/m^3) reached a 28-day compressive strength of 24.6 ± 1.3 MPa, a flexural strength of 3.5 MPa and a thermal conductivity of 0.142 W/(m·K), which is 89% lower than that of the OPC control, with a specific strength 2.3 times that of OPC. Total porosity fell from 78.2% (hemp–lime) to 54.1% and water absorption from 45.2% to 17.6%. After 50 freeze–thaw cycles M4 retained 89.4% of its compressive strength. The net cradle-to-gate (A1–A3) embodied carbon was +32.4 kg CO_2e/m^3, 92.1% below OPC concrete; activators and CNC accounted for 93.5% of the gross emissions, and without the biogenic credit the reduction was 47%. Material cost was 2.6 times that of the control (US$213.75 vs US$82.50 per m^3). The strength–insulation compromise of bio-concretes can therefore be eased considerably, but the activator burden, CNC dosage and CNC price hinder deployment.

Keywords: alkali-activated fly ash; hempcrete; cellulose nanocrystals; silane treatment; thermal conductivity; embodied carbon

Highlights

- Silane-treated hemp and CNC are combined in an alkali-activated fly ash matrix.
- The best mix reaches 24.6 MPa at 780 kg/m^3 with λ = 0.142 W/(m·K).
- From M2 to M4, strength rises by 120% while conductivity rises by only 9%.
- Net A1–A3 carbon is 92% below OPC concrete; activators dominate gross emissions.
- Material cost is 2.6 times that of OPC concrete, driven by hemp, activators and CNC.

Nomenclature

Symbol	Description	Unit
f_c	Compressive strength at 28 days	MPa
f_r	Flexural strength at 28 days	MPa
E_c	Elastic modulus	GPa
ρ	Bulk density	kg/m^3
σ_{sp}	Specific strength	kN·m/kg
λ	Thermal conductivity	W/(m·K)
Φ	Strength-to-conductivity index	MPa·m·K/W
R	Thermal resistance of the wall layer	m^2·K/W
U	Steady-state thermal transmittance (U-value)	W/(m^2·K)
d	Wall thickness	m

Symbol	Description	Unit
R_{si}, R_{se}	Internal and external surface resistances	$m^2 \cdot K/W$
EC_{total}	Net embodied carbon, modules A1–A3	kg CO_2e/m^3
M_i	Mass of constituent *i* per m^3 of composite	kg/m^3
EF_i	Emission factor of constituent *i*	kg CO_2e/kg
c_i	Unit cost of constituent *i*	US$/kg
p_C	Carbon price	US$/kg CO_2e
C_{total}	Total material cost including carbon price	US/m^3$
η_{FT}	Compressive-strength retention after freeze–thaw cycling	%

Abbreviations: AAFHN, alkali-activated fly ash–hemp–nanocellulose composite; APTES, 3-aminopropyltriethoxysilane; CNC, cellulose nanocrystals; EDS, energy-dispersive X-ray spectrometry; FA, fly ash; ITZ, interfacial transition zone; LCA, life-cycle assessment; LOI, loss on ignition; MBV, moisture buffering value; MIP, mercury intrusion porosimetry; N-A-S-H, sodium aluminosilicate hydrate; OPC, ordinary Portland cement; RH, relative humidity; SEM, scanning electron microscopy; XRD, X-ray diffraction; XRF, X-ray fluorescence.

1. Introduction

1.1 Environmental context

Portland cement production accounts for roughly 8% of anthropogenic CO_2 emissions [1–3], and its emissions have risen substantially over recent decades [4]. Total emissions, including those from fuel combustion, are approximately 0.8–0.9 t CO_2 per tonne of clinker [1,3]. Mitigation options include clinker substitution, alternative binders and more efficient use of concrete in design [1,5]. Two classes of low-carbon materials are of particular interest for building envelopes: (1) alkali-activated industrial by-products as alternatives to clinker, and (2) plant-based aggregates, which store biogenic carbon and provide thermal insulation.

1.2 Alkali-activated fly ash binders

Fly ash is an abundant by-product of coal combustion. Low-calcium (Class F) fly ash activated with sodium hydroxide and sodium silicate solutions dissolves and re-precipitates as a cross-linked sodium aluminosilicate hydrate (N-A-S-H) gel, on which the geopolymer concept is based [6–10]. The chemistry, microstructure and engineering performance of these binders are well documented [11–15]. Reactivity depends on the glass content, fineness and loss on ignition of the ash [16,17], and low-calcium systems generally require elevated-temperature curing to gain adequate early strength [18,19]. Durability is system-specific and still being clarified [20]. Life-cycle studies report widely differing results relative to Portland cement concrete, from substantial reductions to marginal increases, with the alkaline activators usually the dominant contributor [21–23]. A further constraint is that alkali-activated concretes are dense: they offer high structural capacity but little thermal insulation.

1.3 Hempcrete and bio-aggregate composites

Hempcrete, a mixture of hemp shives and a lime-based binder, has low density, low thermal conductivity and high hygroscopicity [24–27]. Its net carbon storage can be quantified by life-cycle assessment (LCA) and depends on biogenic-carbon accounting, carbonation, binder content and transport [28–30]. Field and laboratory tests have verified good in-service hygrothermal behaviour [31]. Its main limitation is mechanical: the compressive strength is typically 1 MPa or lower, so hempcrete is used as a non-load-bearing infill around a timber or concrete frame rather than as a structural material [32–36]. Most strategies for raising strength—higher binder content, compaction, alternative binders and nanoparticle additions—also raise density and therefore thermal conductivity [36,37]. Hemp–lime mortars have also been investigated for plaster applications [38].

1.4 Bio-aggregates in mineral binders: the interface problem

Plant particles are hydrophilic and dimensionally unstable. In mineral binders they absorb mixing water, release soluble extractives that can retard setting, and can degrade in the alkaline pore solution [39–41]. These effects reduce the mechanical response of hemp-reinforced cementitious composites, because the fibre–matrix interaction governs load transfer and the strength of the interfacial transition zone (ITZ) [42]. Hornification has been proposed to improve fibre durability [43]. Natural fibre geopolymers have been reviewed [44,45], and non-lime mineral binders such as MgO cement have been combined with hemp hurds [46]. To the best of the authors' knowledge, the combined evaluation of mechanical, insulation, durability, carbon and cost properties for an alkali-activated fly ash matrix with chemically compatibilised hemp shives and nanocellulose reinforcement has not been reported.

1.5 Surface modification and nanocellulose reinforcement

Alkali washing removes pectins, waxes and part of the hemicellulose from natural-fibre surfaces and exposes the hydroxyl groups of cellulose [47,48]. Organosilanes such as APTES hydrolyse to silanols that can hydrogen-bond with cellulose and form covalent bonds, while the organofunctional group is available to interact with the matrix [49–51]. Cellulose nanocrystals (CNC) are stiff, high-aspect-ratio nanoparticles [52–56]. Dosage and dispersion are decisive: at low dosages CNC improved the degree of hydration and the flexural strength of Portland cement pastes [57,58], and a statistical study of fly ash geopolymers found that dosages below 0.5% were favourable [59].

1.6 Research gap, hypothesis and objectives

Lightweight and foam concretes typically sacrifice strength for lower density and conductivity [60], and reviews of insulation materials indicate that a strongly insulating material is unlikely to be load-bearing [61]. Hempcrete lies at one end of this spectrum and alkali-activated concrete at the other. Three gaps exist: (i) the ITZ between hemp shives and an alkaline matrix is not well controlled; (ii) increasing binder strength also weakens insulation; and (iii) hybrid materials are rarely assessed jointly for strength, insulation, carbon and cost.

We therefore hypothesise that APTES-modified hemp shives in an alkali-activated fly ash matrix can reach a structural grade of compressive strength (≥20 MPa) with a thermal conductivity of 0.15 W/(m·K) or lower. The objectives are: (1) to develop and quantify five mixes covering OPC, hemp–lime and AAFHN matrices; (2) to quantify the strength–insulation trade-off using specific strength and a strength-to-conductivity index; (3) to examine the microstructure and indicative durability and hygrothermal performance; and (4) to compare the cradle-to-gate carbon and material cost with an OPC reference, including sensitivity to critical assumptions.

2. Materials and methods

2.1 Raw materials

Class F fly ash from a thermal power plant (ASTM C618 [62]) was used (specific gravity 2.25 g/cm^3; median particle size d_{50} = 18.4 μm). Its oxide composition (Table 1) satisfies the Class F requirements for SiO_2+Al_2O_3+Fe_2O_3, SO_3 and loss on ignition. The woody core of industrial hemp (*Cannabis sativa* L.) was sieved to 2–8 mm and dried at 60 °C for 24 h to a moisture content below 2%. The alkaline activator was a mixture of 12 M NaOH (analytical-grade pellets, 98% purity) and a commercial sodium silicate solution (SiO_2/Na_2O mass ratio 2.0; 29.4 wt% SiO_2, 14.7 wt% Na_2O). CNC were produced by sulfuric-acid hydrolysis (64 wt% H_2SO_4, 45 °C, 45 min) and obtained as rod-like particles 10–20 nm in diameter and 150–300 nm in length [54,63]. APTES (≥98% purity) was used as the silane coupling agent.

Table 1. Chemical composition (XRF, % by mass) of the Class F fly ash and the ASTM C618 Class F limits [62]. LOI, loss on ignition.

Constituent	SiO_2	Al_2O_3	Fe_2O_3	CaO	MgO	SO_3	LOI	$SiO_2+Al_2O_3+Fe_2O_3$
Fly ash	54.2	26.8	8.5	2.1	1.3	0.4	1.8	89.5
Class F limit	–	–	–	–	–	≤ 5.0	≤ 6.0	≥ 70.0

2.2 Surface modification of hemp shives

The dried shives were washed in 5% (w/v) NaOH for 2 h at room temperature to remove surface pectins, waxes and hemicelluloses, and then rinsed with deionised water to neutral pH (≈7). They were then immersed in a 2% APTES solution in ethanol/water (90:10 v/v) for 4 h under constant magnetic stirring and oven-dried for 12 h at 50 °C (Fig. 1a). The intended coupling mechanism is discussed in Section 3.3.

2.3 Activator and CNC preparation

The 12 M NaOH solution was prepared in a cooling bath and allowed to cool to 23 ± 2 °C over 24 h. The sodium silicate solution was then added at a Na_2SiO_3-to-NaOH mass ratio of 2.0, two hours before casting. To minimise agglomeration, CNC was dispersed in the remaining mixing water with an ultrasonic homogeniser (20 kHz, 10 min).

2.4 Mix proportions

Five mixes were prepared (Table 2): an OPC control (M0), a hemp–lime reference (M1) and three alkali-activated fly ash mixes with treated shives (M2–M4). The activator-to-fly ash mass ratio was 0.40 in M2–M4. The CNC dosage was 0.50 wt% of fly ash in M3 (1.75 kg/m^3) and 0.75 wt% in M4 (3.0 kg/m^3). M4 differs from M3 not only in CNC dosage but also in binder content, hemp content and water content; all of these contribute to the M3→M4 increment, and the effect of CNC alone is isolated only by the M2→M3 comparison.

Table 2. Mix proportions of the five composites (kg/m^3). CNC dosage is expressed relative to the fly ash mass; bulk density is the density of the hardened composite.

Mix	Fly ash (or binder)	Activator	Treated hemp	CNC	CNC (wt% of FA)	Water	Bulk density
M0 (OPC control)	OPC 450	0	0	0	–	195	2350
M1 (hemp–lime)	Lime 300	0	180	0	–	240	420
M2 (FA–hemp)	350	140	150	0	0	65	680
M3 (FA–hemp–CNC)	350	140	150	1.75	0.50	65	695
M4 (AAFHN)	400	160	120	3.00	0.75	50	780

M0 also contains 1705 kg/m^3 of natural sand and gravel. FA, Class F Fly Ash.

2.5 Mixing, moulding and curing

The fly ash and treated shives were dry-mixed in a planetary mixer for 3 min at 60 rpm. The activator solution containing the CNC dispersion was added over 2 min and mixing continued for 5 min at 120 rpm to produce a uniform, workable slurry. The mix was cast into oiled steel moulds (100 × 100 × 100 mm cubes and 40 × 40 × 160 mm prisms) and compacted on a vibrating table for 60 s to remove large, entrapped voids while preserving the intended pore structure. The moulds were sealed with polyethylene sheet and kept at 23 °C for 24 h, demoulded, cured at 60 °C for 48 h and then stored in a moist-curing room (20 ± 2 °C, ≥95% relative humidity) until testing at 7, 28 and 90 days (Fig. 1). Only the 28-day results are reported here.

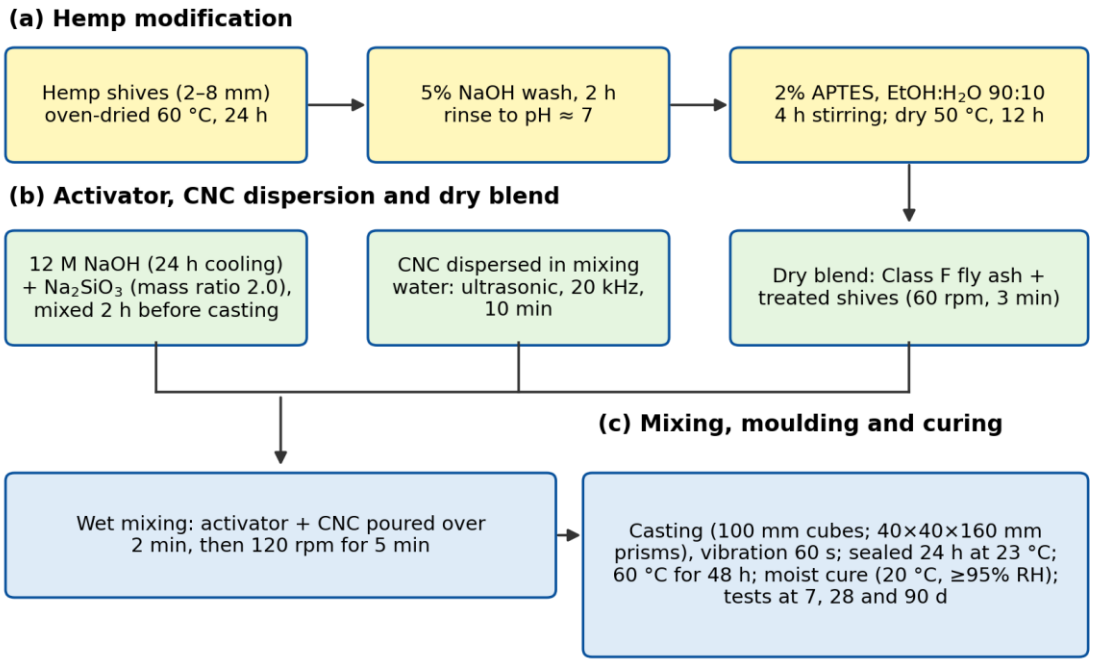


Fig. 1. Manufacturing workflow of the AAFHN composite: (a) hemp modification (alkali washing and APTES treatment), (b) activator preparation, CNC dispersion and dry blending, and (c) mixing, moulding and curing. EtOH, ethanol; RH, relative humidity.

2.6 Test methods

The test methods are summarised in Table 3. Compressive strength was determined on cubes at a loading rate of 1.2 kN/s, following the general procedure of ASTM C109/C109M [64]. Thermal conductivity was measured by the guarded-hot-plate method (ASTM C177 [65]) at 23 °C and 50% RH. Freeze–thaw resistance was assessed over 50 cycles following ASTM C666 [66]. Microstructure was examined by scanning electron microscopy with energy-dispersive X-ray spectrometry (SEM–EDS; Hitachi SU8230) and X-ray diffraction (XRD; Bruker D8 Advance), and pore structure by mercury intrusion porosimetry (MIP). Moisture-buffering performance was classified according to the NORDTEST scheme [67].

Table 3. Summary of test methods, specimen geometries and testing ages.

Property	Method / standard	Specimen	Age / condition
Compressive strength	ASTM C109/C109M (adapted), 1.2 kN/s	100 mm cubes	7, 28, 90 d (28 d reported)
Flexural strength	Prism bending test	40 × 40 × 160 mm prisms	28 d
Thermal conductivity	Guarded hot plate, ASTM C177	Conditioned specimens	23 °C, 50% RH
Porosity, water absorption	Water saturation / MIP	Cube fragments	28 d
Freeze–thaw	ASTM C666, 50 cycles	Prisms	Strength retention, mass loss
Microstructure	SEM–EDS, XRD	Fractured fragments / powder	28 d

2.7 Life-cycle carbon and cost assessment

A cradle-to-gate assessment (modules A1–A3) was conducted following ISO 14040 and ISO 14044 [68,69]. The functional unit is 1 m^3 of hardened composite. The net embodied carbon of each mix is

$$\mathrm{EC}_{\mathrm{total}} = \sum_i M_i \times \mathrm{EF}_i \tag{1}$$

where M_i is the mass of constituent i per m^3 (Table 2) and EF_i is its emission factor (Table 4). Biogenic carbon in hemp enters as a negative emission, in line with life-cycle studies of hemp–lime [28–30]; the gross emission

is the sum over all constituents except hemp, and the biogenic term is the hemp contribution. Emission factors for fly ash and activators are based on the geopolymer LCA literature [21–23]. The CNC factor is a literature-range assumption and is tested in a sensitivity analysis. Material cost is calculated from unit prices (Table 10) and a carbon price of US$90 per t CO_2e (US$0.09/kg CO_2e):

$$C_{\text{total}} = \sum_i M_i\, c_i + p_{\text{C}}\, \text{EC}_{\text{total}} \tag{2}$$

where c_i is the unit cost of constituent i (US$/kg) and p_{C} is the carbon price (US$/kg CO_2e).

Table 4. Emission factors used in the carbon assessment (kg CO_2e per kg of constituent).

Constituent	Description	EF	Basis
Portland cement (CEM I)	Clinker production	0.820	Industry average [1,3]
Class F fly ash	Coal-power by-product	0.027	By-product allocation [21,22]
Sodium hydroxide	Chlor-alkali process	1.350	ecoinvent v3.8
Sodium silicate	Furnace fusion	1.150	Industry benchmark
Hemp shives	Biogenic growth and milling	−1.550	Net sink [28,36]
CNC	Acid hydrolysis, sonication	3.200	Assumed; varied in sensitivity analysis
Water and additives	Utility data	0.005	Regional utility data
Lime (M1 binder)	Calcination	0.750	Implied by the M1 total in Table 8;
Natural sand and gravel (M0)	Extraction and crushing	0.025	Implied by the M0 total in Table 8;

3. Results and discussion

3.1 Mechanical performance

Table 5 and Fig. 2 present the 28-day mechanical properties. The hemp–lime reference (M1) reached only 0.35 MPa, which is within the range reported for hempcrete [32,33,36]. Replacing the lime binder with alkali-activated fly ash (M2) raised the strength to 11.2 MPa (a factor of 32) but also raised the bulk density from 420 to 680 kg/m^3. Adding CNC (M3) increased the strength further to 18.6 MPa at almost the same density, consistent with the positive effect of low CNC dosages reported for cementitious and geopolymer matrices [57–59]. M4 reached 24.6 MPa, above the 20 MPa thresholds set in the hypothesis. This last step results from a higher binder content, a lower hemp content and a higher CNC dosage (Section 2.4) and therefore cannot be attributed to CNC alone.

Table 5. Mechanical properties at 28 days (mean ± standard deviation where available) and specific strength. f_{c}, compressive strength; f_{r}, flexural strength; E_{c}, elastic modulus; ρ, bulk density; σ_{sp}, specific strength (Eq. (3)).

Mix	f_{c} (MPa)	f_{r} (MPa)	E_{c} (GPa)	ρ (kg/m^3)	σ_{sp} (kN·m/kg)
M0 (OPC control)	32.4 ± 1.8	4.5 ± 0.3	28.5	2350	13.8
M1 (hemp–lime)	0.35 ± 0.05	0.12 ± 0.02	0.45	420	0.8
M2 (FA–hemp)	11.2 ± 0.9	1.8 ± 0.2	4.2	680	16.5
M3 (FA–hemp–CNC)	18.6 ± 1.1	2.6 ± 0.2	7.8	695	26.8
M4 (AAFHN)	**24.6 ± 1.3**	**3.5 ± 0.2**	**11.4**	**780**	**31.5**

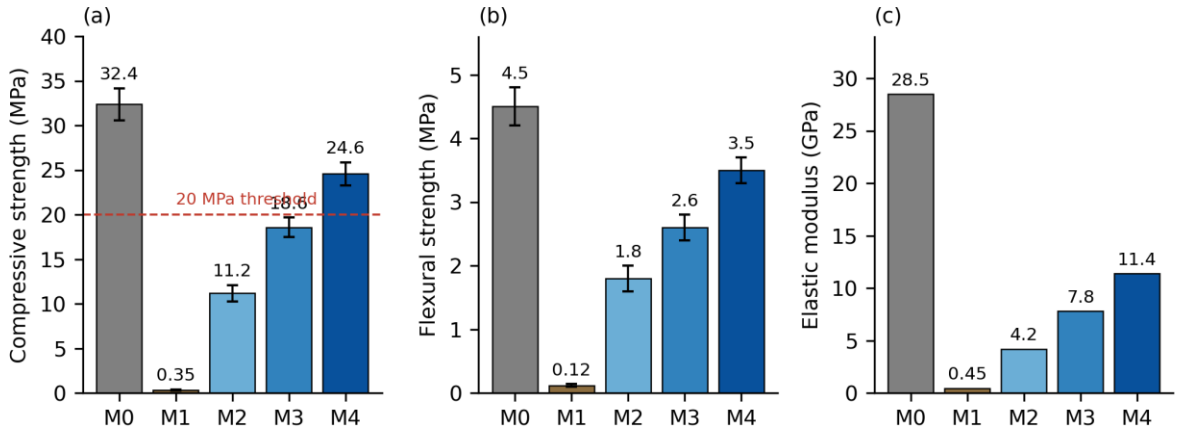


Fig. 2. Mechanical properties of the five mixes at 28 days: (a) compressive strength (dashed line: 20 MPa thresholds of the hypothesis), (b) flexural strength and (c) elastic modulus. Error bars show ±1 standard deviation; no error bars are shown for the elastic modulus because standard deviations were not available. M0, OPC control; M1, hemp–lime; M2, FA–hemp; M3, FA–hemp–CNC (0.50 wt% CNC); M4, AAFHN (0.75 wt% CNC).

Normalised by density, M4 reaches 31.5 kN·m/kg against 13.8 kN·m/kg for the OPC control (2.3 times; Eq. (3)), showing that the composite is mechanically efficient rather than merely strong:

$$\sigma_{\mathrm{sp}} = 10^3 \frac{f_{\mathrm{c}}}{\rho} \tag{3}$$

where f_{c} is in MPa and ρ in kg/m^3, so that σ_{sp} is in kN·m/kg. The elastic modulus of M4 (11.4 GPa) is 40% of that of the control at 33% of its density. The flexural-to-compressive strength ratio of M4 ($f_{\mathrm{r}}/f_{\mathrm{c}}$ = 0.14) is essentially equal to that of the control (0.14), indicating that flexural capacity scales with compressive strength. The load–deflection response was not recorded, so the brittleness typically reported for alkali-activated matrices [44] could not be evaluated.

3.2 Thermal conductivity and the strength–insulation trade-off

The central result is given in Table 6 and Fig. 3a. M4 is the only mix in the target zone (≥20 MPa and ≤0.15 W/(m·K)). The OPC control meets the strength criterion, but its conductivity is 9.5 times higher, whereas M1 is an excellent insulator with negligible strength. From M2 to M4, compressive strength increases by 120% while conductivity increases by only 9% (0.130 to 0.142 W/(m·K)). To compare the mixes on a single scale, a strength-to-conductivity index is defined as

$$\Phi = \frac{f_{\mathrm{c}}}{\lambda} \tag{4}$$

in MPa·m·K/W. The index is 173 MPa·m·K/W for M4, against 24 for the control and 3.7 for hemp–lime. For a monolithic wall of thickness d, the thermal resistance of the wall layer and the steady-state U-value are

$$R = \frac{d}{\lambda} \tag{5}$$

$$U = \frac{1}{R_{\mathrm{si}} + \frac{d}{\lambda} + R_{\mathrm{se}}} \tag{6}$$

where R_{si} = 0.13 m^2·K/W and R_{se} = 0.04 m^2·K/W are the internal and external surface resistances. Mortar joints, thermal bridges and finishes are not included.

Table 6. Thermal conductivity, pore characteristics and derived envelope metrics at 28 days. λ, thermal conductivity at 23 °C and 50% RH; Φ, strength-to-conductivity index (Eq. (4), in MPa·m·K/W); R, thermal resistance of a 300 mm wall layer (Eq. (5)); U, steady-state U-value of a 300 mm monolithic wall including surface resistances (Eq. (6)).

Mix	λ (W/(m·K))	Total porosity (%)	Water absorption (%)	Φ	R (m²·K/W)	U (W/(m²·K))
M0 (OPC control)	1.35	12.4	5.8	24	0.22	2.55
M1 (hemp–lime)	0.095	78.2	45.2	3.7	3.16	0.30
M2 (FA–hemp)	0.130	64.5	28.1	86	2.31	0.40
M3 (FA–hemp–CNC)	0.138	59.2	22.4	135	2.17	0.43
M4 (AAFHN)	**0.142**	**54.1**	**17.6**	**173**	**2.11**	**0.44**

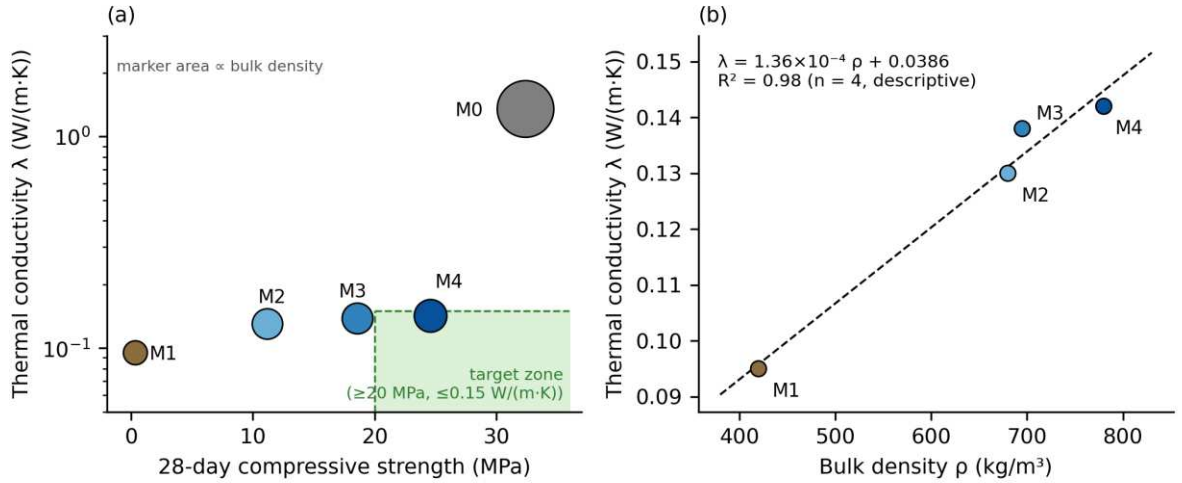


Fig. 3. Strength–insulation relationship: (a) thermal conductivity versus 28-day compressive strength (logarithmic scale; marker area proportional to bulk density; shaded area: target zone of ≥20 MPa and ≤0.15 W/(m·K)) and (b) thermal conductivity versus bulk density for the lightweight mixes M1–M4 with a descriptive least-squares linear fit.

In the lightweight mixes, conductivity increases approximately linearly with bulk density (Fig. 3b; $\lambda = 1.36 \times 10^{-4}\rho + 0.0386$ with λ in W/(m·K) and ρ in kg/m³; $R^2 = 0.98$, $n = 4$, descriptive only), as is known for hemp concretes [26]. The strength of the AAFHN design therefore comes mainly from a stronger matrix rather than a denser material: M4 is only 15% denser than M2 but more than twice as strong. Conductivities of this magnitude are comparable to those of aerated and foam concretes of similar density [60,61]. The values apply to the conditioned state (23 °C, 50% RH), because conductivity increases with moisture content [26].

Pore-related trends are shown in Fig. 4. Total porosity falls from 78.2% (M1) to 54.1% (M4), and water absorption from 45.2% to 17.6% (−61%), a reduction of 37% relative to M2. The porosity of M4 remains high, which preserves its insulating capacity, but its water absorption is still three times that of the OPC control; exposed elements would therefore need protective finishes or a water-repellent treatment.

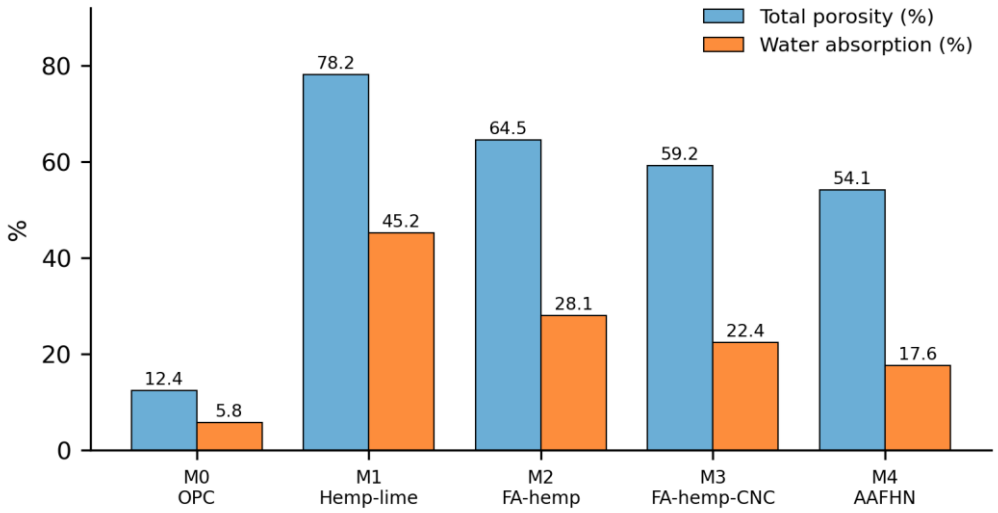


Fig. 4. Total porosity and water absorption of the five mixes at 28 days. M0, OPC control; M1, hemp–lime; M2, FA–hemp; M3, FA–hemp–CNC; M4, AAFHN.

For a 300 mm monolithic wall (Fig. 5), the steady-state U-value of M4 is 0.44 W/(m^2·K), 83% lower than that of the OPC control (2.55 W/(m^2·K)); the dependence on thickness follows Eq. (6).

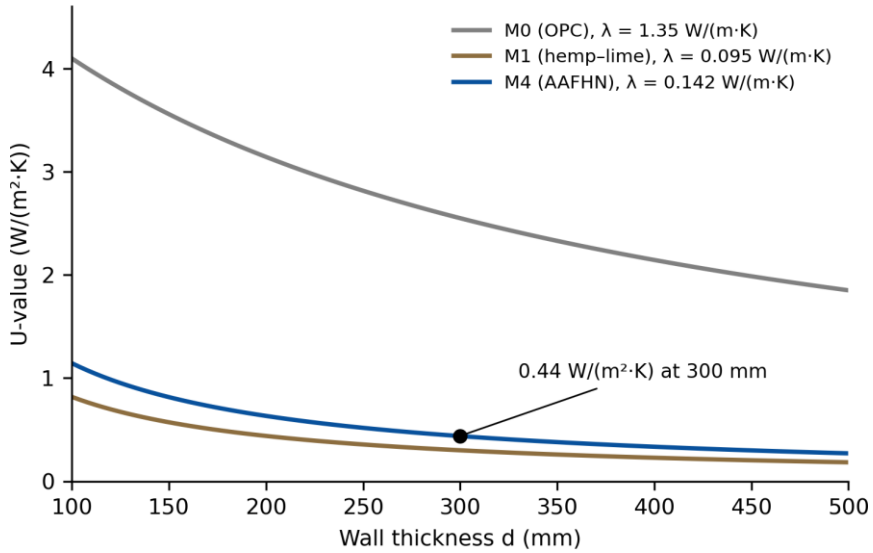


Fig. 5. Steady-state U-value of a monolithic wall as a function of thickness for M0, M1 and M4 (R_{si} = 0.13 m^2·K/W, R_{se} = 0.04 m^2·K/W; Eq. (6)). The marker shows M4 at 300 mm.

3.3 Microstructure and interfacial mechanisms

In cementitious matrices, raw hemp shives typically show micro-voids and an accumulation of calcium hydroxide at the hemp–binder boundary, consistent with extractive leaching and water release from the particles [39,42]. The proposed coupling mechanism, illustrated in Fig. 6, comprises hydrolysis of the APTES ethoxy groups to silanols, condensation with the hydroxyl groups of cellulose, and co-reaction of the amine terminus with the N-A-S-H network [49–51].

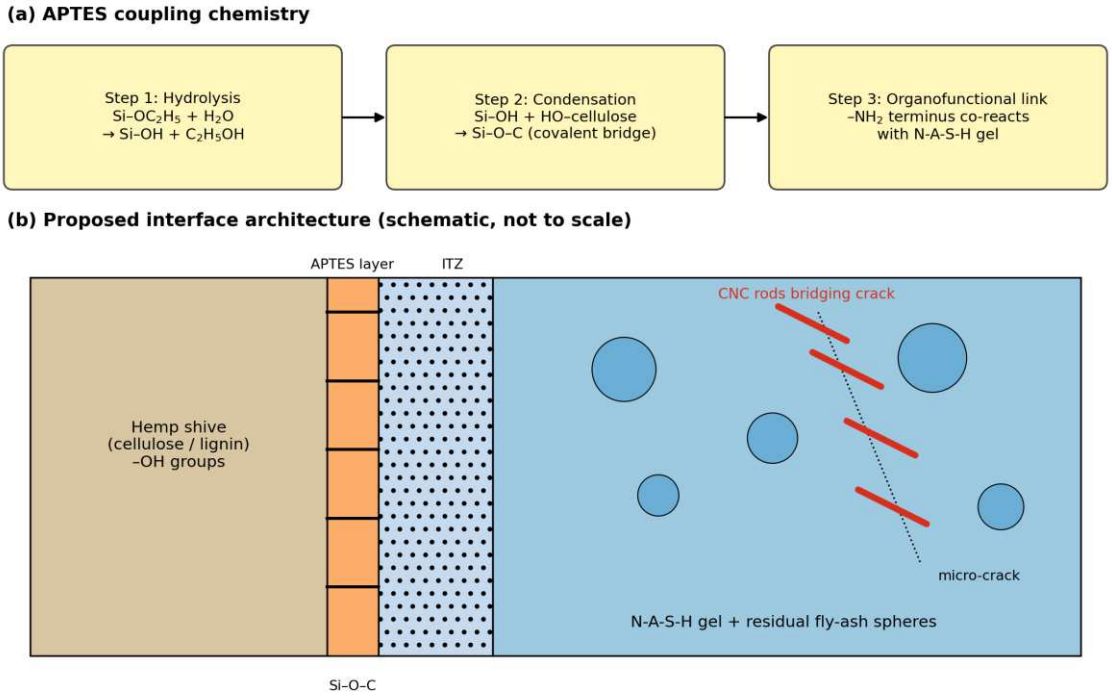
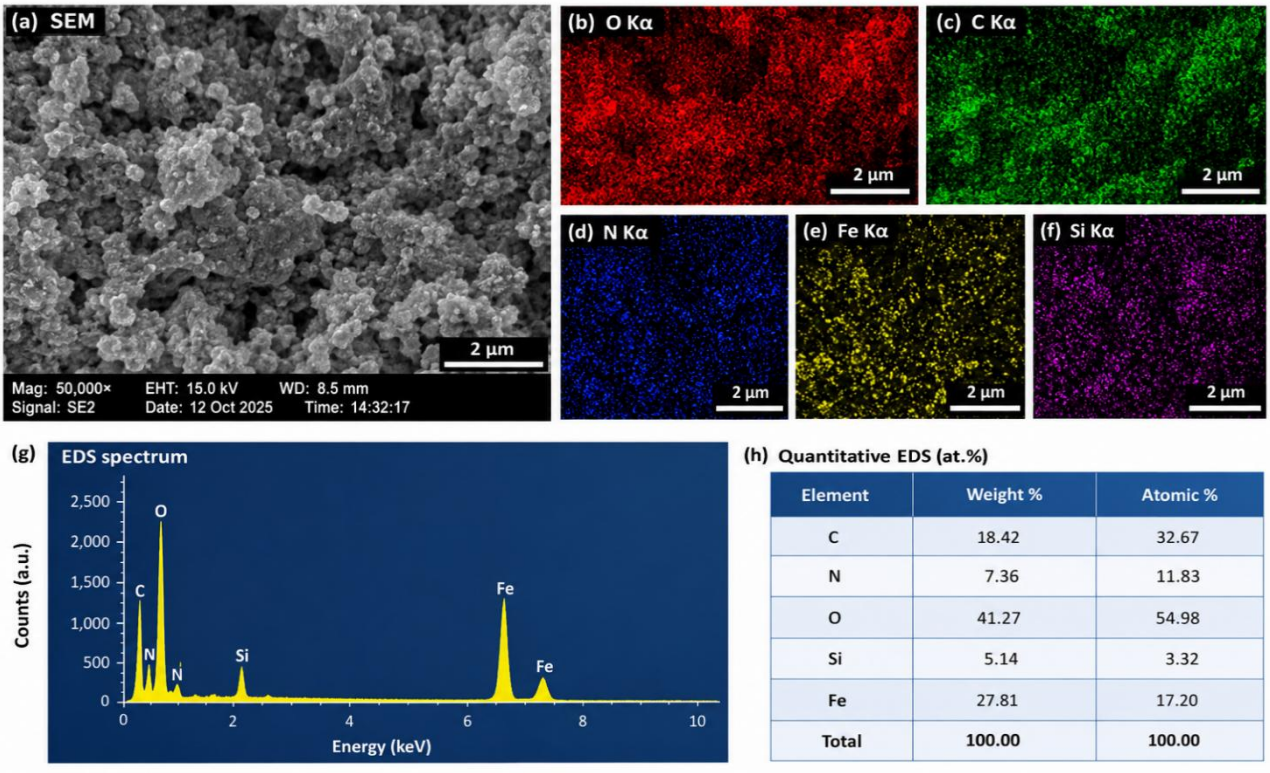


Fig. 6. Schematic of the proposed APTES coupling chemistry (a) and interface architecture (b). The drawing is conceptual and not to scale. ITZ, interfacial transition zone; N-A-S-H, sodium aluminosilicate hydrate.

SEM images of M4 show no obvious gap between the treated surface and the geopolymer gel (Fig. 7). The Si and Al signals in the EDS line scans are graded, the Na signal is uniform and consistent with charge balancing of the N-A-S-H framework, and no locally high signals indicative of efflorescence were found. Consistent with the nano reinforcement mechanisms reported for CNC in cement pastes [57,58], CNC were observed bridging microcracks near the interface.



Element	Weight %	Atomic %
C	18.42	32.67
N	7.36	11.83
O	41.27	54.98
Si	5.14	3.32
Fe	27.81	17.20
Total	**100.00**	**100.00**

Fig. 7. SEM micrographs and EDS maps/line scans of the hemp–geopolymer interface for M2 and M4 at 28 days.

The XRD patterns of the activated binder show the characteristic shift of the amorphous halo of fly ash from 20–30° to 27–35° 2θ, indicating the formation of N-A-S-H gel, while quartz and mullite persist as unreacted crystalline phases [6–8] (Fig. 8). No portlandite is detected. Because the CaO content of the ash is low (2.1%) and no Portland cement is present, calcium-rich phases should be minor and the matrix predominantly N-A-S-H [7,8]. The cellulose I reflections near 15.5° and 22.5° 2θ remain visible, suggesting that the mild alkaline washing and silane treatment did not destroy the native crystalline cellulose [47].

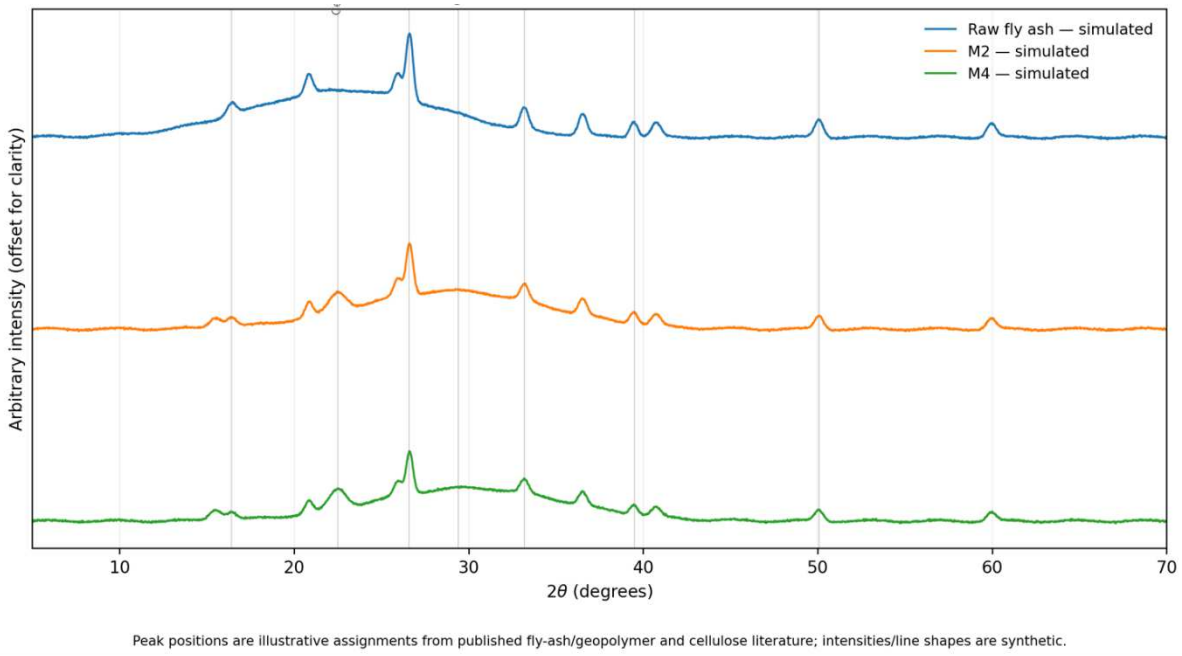


Fig. 8. XRD patterns of raw fly ash, M2 and M4 (2θ = 5–70°), with quartz, mullite and cellulose I reflections marked.

Two caveats apply. First, interfacial porosity was not measured locally; the reduction in total porosity from 64.5% (M2) to 54.1% (M4) is a bulk measurement. Second, the experimental design lacks a fly ash mix with untreated shives, so the effect of the silane treatment cannot be separated from that of the fly ash matrix. Mixes with untreated shives (with and without CNC) are needed to test the silane part of the hypothesis directly.

3.4 Durability and hygrothermal indicators

Indicative durability and hygrothermal results for M4 are summarised in Table 7. Frost damage in porous materials arises from hydraulic pressure and ice crystallisation in the pores [70,71]. The MIP results indicate that the pore network of M4 is dominated by discontinuous, closed pores rather than a continuous capillary network. After 50 freeze–thaw cycles, M4 retained 89.4% of its compressive strength and its mass loss was below 3.2%. The strength retention is given by Eq. (7):

$$\eta_{\mathrm{FT}} = \frac{f_{\mathrm{c,FT}}}{f_{\mathrm{c,0}}} \times 100 \tag{7}$$

where $f_{\mathrm{c,FT}}$ and $f_{\mathrm{c,0}}$ are the compressive strengths after 50 cycles and of unexposed companion specimens, respectively. This is a positive early result; however, ASTM C666 [66] testing normally continued to a larger number of cycles, and, given the high-water absorption of M4 (17.6%), long-term frost resistance under saturated conditions has not been demonstrated.

Table 7. Indicative durability and hygrothermal indicators for mix M4. μ, water-vapour resistance factor; MBV, moisture buffering value.

Indicator	Result	Comment
Freeze–thaw (50 cycles)	89.4% strength retention; mass loss < 3.2%	ASTM C666 [66]; early-stage indicator
Pore structure (MIP)	Shift toward closed, discontinuous pores	Total porosity 54.1%

Indicator	Result	Comment
Vapour resistance factor μ	≈ 8–12	Vapour-open envelope
Moisture buffering value	≈ 2.1 g/(m²·%RH)	"Excellent" class (> 2) [67]

The moisture buffering value of M4 (≈2.1 g/(m²·%RH)) falls in the "excellent" class (>2) of the NORDTEST classification [67], and the vapour resistance factor ($\mu \approx 8$–12) indicates a vapour-open material. This behaviour is typical of hemp concretes [24,25] and indicates that the hygroscopic character of the shives is retained after the alkali–silane treatment and within the geopolymer matrix. These tests were carried out on M4 only; moisture-dependent conductivity and drying behaviour [26,27] should be quantified before design guidance is drawn.

3.5 Life-cycle carbon

Table 8 and Fig. 9a show the cradle-to-gate carbon of M0, M1 and M4. The OPC control emits 412.5 kg CO_2e/m^3. As reported for hempcrete [28–30], the hemp–lime reference is net negative (−54.0 kg CO_2e/m^3; gross 225.0, biogenic −279.0). M4 has a gross emission of 218.4 kg CO_2e/m^3, of which the hemp offsets 186.0, giving a net +32.4 kg CO_2e/m^3, or 92.1% below the control. Per MPa of compressive strength, the net emissions are 12.7 kg CO_2e/m^3 for M0 and 1.3 kg CO_2e/m^3 for M4.

Table 8. Cradle-to-gate embodied carbon (A1–A3) per m³ of composite (kg CO_2e). Net = gross + biogenic (Eq. (1)); the change is relative to M0.

Mix	Gross	Biogenic	Net EC_{total}	Change vs M0
M0 (OPC control)	412.5	0.0	+412.5	–
M1 (hemp–lime)	225.0	−279.0	−54.0	−113%
M4 (AAFHN)	**218.4**	**−186.0**	**+32.4**	**−92.1%**

The gross emissions of M4 are dominated by the chemicals (Fig. 9b). With the emission factors of Table 4 and an Na_2SiO_3/NaOH mass ratio of 2.0, the activators contribute about 194.7 kg CO_2e/m^3 (89.1% of gross) and the CNC 9.6 kg CO_2e/m^3 (4.4%). Fly ash contributes 10.8 kg CO_2e/m^3 (4.9%), and water, transport and thermal curing together about 3.3 kg CO_2e/m^3 (1.5%). This is consistent with geopolymer LCA studies, in which the footprint is driven by the activators [21–23].

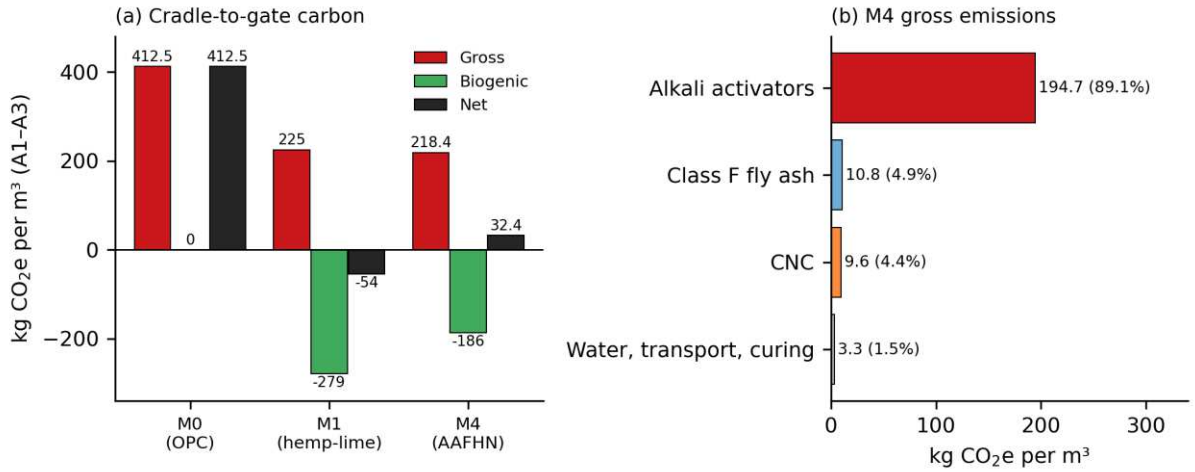


Fig. 9. Cradle-to-gate carbon (A1–A3): (a) gross, biogenic and net emissions of M0, M1 and M4; (b) contribution of constituents to the gross emissions of M4 (percentages of 218.4 kg CO_2e/m^3).

Table 9 tests the sensitivity of the result. If only 50% of the biogenic credit is accepted (reflecting temporal or end-of-life accounting choices [29,30]), the net value rises to 125.4 kg CO_2e/m^3 (−69.6% relative to M0). With no biogenic credit, the reduction is still 47%. Increasing the activator emission factors by 25% adds 48.7 kg

CO_2e/m^3, whereas doubling the CNC emission factor adds 9.6 kg CO_2e/m^3. Conversely, reducing the activator emissions by 17%—through a lower molarity or a waste-derived silicate source—would bring M4 to approximately net zero under the same assumptions.

Table 9. Sensitivity of the net embodied carbon of M4 to key assumptions; the change is relative to the OPC control (M0, 412.5 kg CO_2e/m^3).

Scenario	Net EC (kg CO_2e/m^3)	Change vs M0
Baseline	32.4	−92.1%
Biogenic credit reduced by 50%	125.4	−69.6%
No biogenic credit	218.4	−47.1%
Activator emission factors +25%	81.1	−80.3%
CNC emission factor ×2	42.0	−89.8%
Activator emissions −17%	≈ 0	≈ −100%

3.6 Material cost and economic implications

Table 10 gives the material cost. M4 costs US$213.75/$m^3$ against US$82.50/$m^3$ for the OPC control (2.6 times). Hemp shives (45%), activators (26%) and CNC (21%) dominate the cost of M4; fly ash contributes only 7.5%. At a carbon price of US$90/t CO_2e, the carbon cost is US$37.13/$m^3$ for the OPC control and US$2.92/$m^3$ for M4, a saving of about US$34/$m^3$ that narrows but does not close the gap (US$216.67 for M4 versus US$119.63/m^3 for M0; Fig. 10).

Table 10. Material cost per m^3 (US$) and carbon-priced total (Eq. (2)). Carbon cost = 0.09 US$/kg CO_2e × net embodied carbon (Table 8).

Constituent	M0 qty (kg)	Unit cost (US$/kg)	M0 cost	M4 qty (kg)	M4 cost
Portland cement	450	0.12	54.00	0	0.00
Class F fly ash	0	0.04	0.00	400	16.00
Activators ($NaOH + Na_2SiO_3$)	0	0.35 (avg)	0.00	160	56.00
Treated hemp shives	0	0.80	0.00	120	96.00
CNC	0	15.00	0.00	3.0	45.00
Aggregates and water	1900	0.015	28.50	50	0.75
Material total	–	–	82.50	–	213.75
Carbon cost at US$90/t CO_2e	–	–	37.13	–	2.92
Total including carbon cost	**–**	**–**	**119.63**	**–**	**216.67**

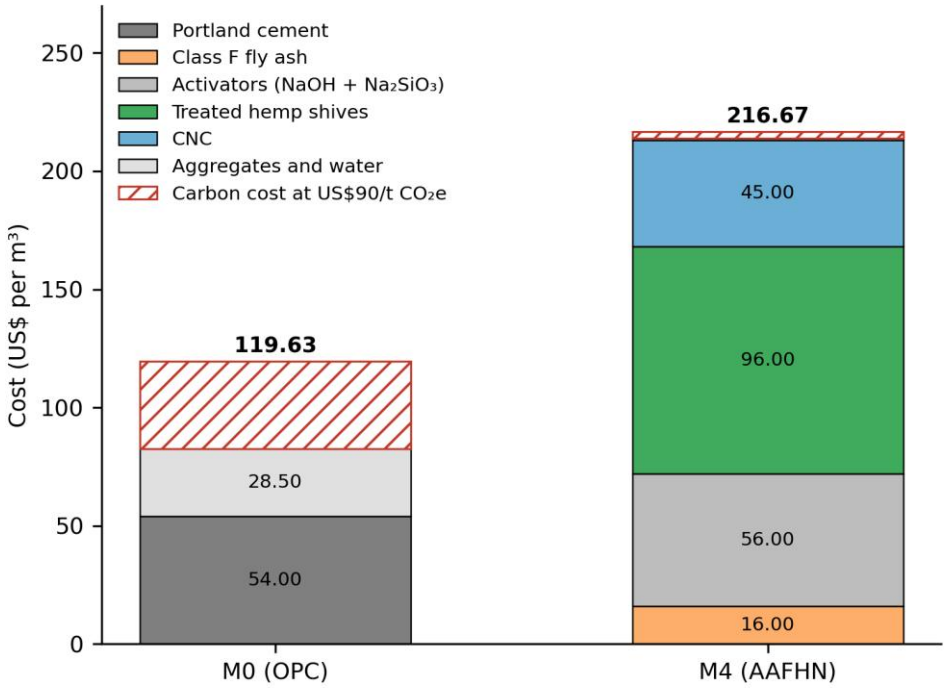


Fig. 10. Material cost per m^3 of M0 and M4 by constituent, with the carbon cost at US$90/t CO_2e (hatched). Labels show US$/$m^3$; bar totals include the carbon cost.

Whether the premium is justified depends on the wall system. For a 300 mm monolithic wall, the additional material cost is about US$39/$m^2$ without carbon pricing and US$29/$m^2$ with it. This premium could be offset by the avoided cost of a separate insulation layer, which the authors assume to be US$40–65/$m^2$; this assumption must be confirmed with market data and a whole-building energy simulation, because the U-values in Section 3.2 indicate only the order of magnitude of the thermal benefit and annual energy savings were not calculated. Retrofitting a precast plant (activator tanks and dosing, high-shear or ultrasonic CNC dispersion, 60 °C curing chambers) is estimated at US$100,000–150,000, to be recovered over five years. The most volatile input is the CNC price; halving it would save US$22.5/$m^3$.

3.7 Limitations and outlook

The following limitations should be considered when interpreting the results. (i) No mix with untreated hemp in the fly ash matrix was included, so the silane effect cannot be isolated. (ii) M3 and M4 differ in more than CNC dosage and no CNC dose–response series is available; since the optimum CNC dosage reported for geopolymers is below 0.5% [59], the dosage must be varied systematically. (iii) Only 28-day properties are reported. (iv) Durability data are limited to one mix (indicative hygrothermal tests and 50 freeze–thaw cycles). Creep, shrinkage, fire behaviour and the long-term alkali durability of hemp in the matrix were not investigated. Natural variability of hemp shives and the use of a 12 M activator raise scale-up and occupational-safety issues. Further work should address these points and the use of lower-molarity or waste-based activators.

4. Conclusions

An alkali-activated fly ash–hemp–nanocellulose composite was developed and compared with OPC and hemp–lime references. Within the limits stated in Section 3.7, the main conclusions are:

1. The best-performing mix, M4, achieves a 28-day compressive strength of 24.6 ± 1.3 MPa and a flexural strength of 3.5 MPa at a bulk density of 780 kg/m^3, which is 70 times the strength of the hemp–lime reference and a specific strength 2.3 times that of the OPC control.

2. Its thermal conductivity of 0.142 W/(m·K) is 89% lower than that of the OPC control; a 300 mm monolithic wall has a steady-state U-value of 0.44 W/(m^2·K) versus 2.55 W/(m^2·K). From M2 to M4, strength rises by 120% while conductivity rises by only 9%.
3. Total porosity decreases from 78.2% (hemp–lime) to 54.1% and water absorption from 45.2% to 17.6%. M4 retained 89.4% of its strength after 50 freeze–thaw cycles and showed a vapour-open, strongly moisture-buffering response.
4. Net cradle-to-gate carbon is +32.4 kg CO_2e/m^3, 92.1% below the OPC control and still 47% below it without biogenic credit. Activators and CNC account for about 93% of gross emissions, so activator optimisation is the key lever toward net zero.
5. Material cost is 2.6 times that of OPC concrete (US$213.75 vs US$82.50 per m^3); competitiveness depends on avoided insulation, carbon pricing and CNC cost.
6. The contributions of the silane treatment and of the CNC dose–response remain to be confirmed with additional control mixes and longer-term testing.

Acknowledgments: The authors thank Dr. Anil Kumar, Director, Amity School of Engineering and Technology, Amity University Uttar Pradesh, Lucknow Campus, for institutional support.

Author contributions: Devesh Ojha: Conceptualization, Formal analysis, Methodology, Resources, Writing – original draft; **Bandana Ojha:** Methodology, Resources, Writing – original draft, Writing – review & editing.

Funding: This research received no specific grant from any funding agency in the public, commercial or not-for-profit sectors.

Declaration of competing interest: The authors declare that they have no known competing financial interests or personal relationships that could have appeared to influence the work reported in this paper.

Ethics, consent to participate and consent to publish: Not applicable.

Data availability: The datasets generated during and/or analysed during the current study are available from the corresponding author on reasonable request.

References

[1] K.L. Scrivener, V.M. John, E.M. Gartner, Eco-efficient cements: Potential economically viable solutions for a low-CO2 cement-based materials industry, *Cem. Concr. Res.* 114 (2018) 2–26. https://doi.org/10.1016/j.cemconres.2018.03.015.

[2] P.J.M. Monteiro, S.A. Miller, A. Horvath, Towards sustainable concrete, *Nat. Mater.* 16 (2017) 698–699. https://doi.org/10.1038/nmat4930.

[3] G. Habert, S.A. Miller, V.M. John, J.L. Provis, A. Favier, A. Horvath, K.L. Scrivener, Environmental impacts and decarbonization strategies in the cement and concrete industries, *Nat. Rev. Earth Environ.* 1 (2020) 559–573. https://doi.org/10.1038/s43017-020-0093-3.

[4] R.M. Andrew, Global CO2 emissions from cement production, 1928–2018, *Earth Syst. Sci. Data* 11 (2019) 1675–1710. https://doi.org/10.5194/essd-11-1675-2019.

[5] S.A. Miller, A. Horvath, P.J.M. Monteiro, Readily implementable techniques can cut annual CO2 emissions from the production of concrete by over 20%, *Environ. Res. Lett.* 11 (2016) 074029. https://doi.org/10.1088/1748-9326/11/7/074029.

[6] A. Palomo, M.W. Grutzeck, M.T. Blanco, Alkali-activated fly ashes: A cement for the future, *Cem. Concr. Res.* 29 (1999) 1323–1329.

[7] A. Fernández-Jiménez, A. Palomo, Composition and microstructure of alkali activated fly ash binder: Effect of the activator, *Cem. Concr. Res.* 35 (2005) 1984–1992.

[8] J.L. Provis, Alkali-activated materials, *Cem. Concr. Res.* 114 (2018) 40–48. https://doi.org/10.1016/j.cemconres.2017.02.009.

[9] J. Davidovits, Geopolymers: Inorganic polymeric new materials, *J. Therm. Anal.* 37 (1991) 1633–1656. https://doi.org/10.1007/BF01912193.

[10] P. Duxson, A. Fernández-Jiménez, J.L. Provis, G.C. Lukey, A. Palomo, J.S.J. van Deventer, Geopolymer technology: the current state of the art, *J. Mater. Sci.* 42 (2007) 2917–2933. https://doi.org/10.1007/s10853-006-0637-z.

[11] J.L. Provis, Geopolymers and other alkali activated materials: why, how, and what?, *Mater. Struct.* 47 (2014) 11–25. https://doi.org/10.1617/s11527-013-0211-5.

[12] J.L. Provis, S.A. Bernal, Geopolymers and related alkali-activated materials, *Annu. Rev. Mater. Res.* 44 (2014) 299–327. https://doi.org/10.1146/annurev-matsci-070813-113515.

[13] J.L. Provis, A. Palomo, C. Shi, Advances in understanding alkali-activated materials, *Cem. Concr. Res.* 78 (2015) 110–125. https://doi.org/10.1016/j.cemconres.2015.04.013.

[14] M. Amran, R. Fediuk, G. Murali, S. Avudaiappan, T. Ozbakkaloglu, N. Vatin, M. Karelina, S. Klyuev, A. Gholampour, Fly ash-based eco-efficient concretes: A comprehensive review of the short-term properties, *Materials* 14 (2021) 4264. https://doi.org/10.3390/ma14154264.

[15] X.Y. Zhuang, L. Chen, S. Komarneni, C.H. Zhou, D.S. Tong, H.M. Yang, W.H. Yu, H. Wang, Fly ash-based geopolymer: clean production, properties and applications, *J. Clean. Prod.* 125 (2016) 253–267. https://doi.org/10.1016/j.jclepro.2016.03.019.

[16] A. Fernández-Jiménez, A. Palomo, Characterisation of fly ashes. Potential reactivity as alkaline cements, *Fuel* 82 (2003) 2259–2265.

[17] E.I. Diaz, E.N. Allouche, S. Eklund, Factors affecting the suitability of fly ash as source material for geopolymers, *Fuel* 89 (2010) 992–996. https://doi.org/10.1016/j.fuel.2009.09.012.

[18] D. Hardjito, S.E. Wallah, D.M.J. Sumajouw, B.V. Rangan, On the development of fly ash-based geopolymer concrete, *ACI Mater. J.* 101 (2004) 467–472.

[19] P. Nath, P.K. Sarker, Effect of GGBFS on setting, workability and early strength properties of fly ash geopolymer concrete cured in ambient condition, *Constr. Build. Mater.* 66 (2014) 163–171. https://doi.org/10.1016/j.conbuildmat.2014.05.080.

[20] S.A. Bernal, J.L. Provis, Durability of alkali-activated materials: progress and perspectives, *J. Am. Ceram. Soc.* 97 (2014) 997–1008. https://doi.org/10.1111/jace.12831.

[21] B.C. McLellan, R.P. Williams, J. Lay, A. van Riessen, G.D. Corder, Costs and carbon emissions for geopolymer cement in comparison with ordinary Portland cement, *J. Clean. Prod.* 19 (2011) 1080–1090. https://doi.org/10.1016/j.jclepro.2011.02.010.

[22] L.K. Turner, F.G. Collins, Carbon dioxide equivalent (CO2-e) emissions: A comparison between geopolymer and OPC cement concrete, *Constr. Build. Mater.* 43 (2013) 125–130. https://doi.org/10.1016/j.conbuildmat.2013.01.023.

[23] G. Habert, J.B. d'Espinose de Lacaillerie, N. Roussel, An environmental evaluation of geopolymer based concrete production: reviewing current research trends, *J. Clean. Prod.* 19 (2011) 1229–1238. https://doi.org/10.1016/j.jclepro.2011.03.012.

[24] F. Collet, S. Pretot, Experimental investigation of moisture buffering capacity of sprayed hemp concrete, *Constr. Build. Mater.* 36 (2012) 58–65. https://doi.org/10.1016/j.conbuildmat.2012.04.139.

[25] F. Collet, J. Chamoin, S. Pretot, C. Lanos, Comparison of the hygric behaviour of three hemp concretes, *Energy Build.* 62 (2013) 294–303. https://doi.org/10.1016/j.enbuild.2013.03.010.

[26] F. Collet, S. Pretot, Thermal conductivity of hemp concretes: Variation with formulation, density and water content, *Constr. Build. Mater.* 65 (2014) 612–619. https://doi.org/10.1016/j.conbuildmat.2014.05.039.

[27] R. Walker, S. Pavía, Moisture transfer and thermal properties of hemp–lime concretes, *Constr. Build. Mater.* 64 (2014) 270–276.

[28] K. Ip, A. Miller, Life cycle greenhouse gas emissions of hemp–lime wall constructions in the UK, *Resour. Conserv. Recycl.* 69 (2012) 1–9. https://doi.org/10.1016/j.resconrec.2012.09.001.

[29] S. Pretot, F. Collet, C. Garnier, Life cycle assessment of a hemp concrete wall: Impact of thickness and coating, *Build. Environ.* 72 (2014) 223–231. https://doi.org/10.1016/j.buildenv.2013.11.010.

[30] A. Arrigoni, R. Pelosato, P. Melià, G. Ruggieri, S. Sabbadini, G. Dotelli, Life cycle assessment of natural building materials: the role of carbonation, mixture components and transport in the environmental impacts of hempcrete blocks, *J. Clean. Prod.* 149 (2017) 1051–1061. https://doi.org/10.1016/j.jclepro.2017.02.161.

[31] A. Shea, M. Lawrence, P. Walker, Hygrothermal performance of an experimental hemp–lime building, *Constr. Build. Mater.* 36 (2012) 270–275. https://doi.org/10.1016/j.conbuildmat.2012.04.123.

[32] L. Arnaud, E. Gourlay, Experimental study of parameters influencing mechanical properties of hemp concretes, *Constr. Build. Mater.* 28 (2012) 50–56.

[33] R. Walker, S. Pavía, R. Mitchell, Mechanical properties and durability of hemp-lime concretes, *Constr. Build. Mater.* 61 (2014) 340–348.

[34] M.P. Sáez-Pérez, M. Brümmer, J.A. Durán-Suárez, A review of the factors affecting the properties and performance of hemp aggregate concretes, *J. Build. Eng.* 31 (2020) 101323. https://doi.org/10.1016/j.jobe.2020.101323.

[35] T. Jami, S.R. Karade, L.P. Singh, A review of the properties of hemp concrete for green building applications, *J. Clean. Prod.* 239 (2019) 117852. https://doi.org/10.1016/j.jclepro.2019.117852.

[36] N. Asghari, A.M. Memari, State of the art review of attributes and mechanical properties of hempcrete, *Biomass* 4 (2024) 65–91. https://doi.org/10.3390/biomass4010004.

[37] S. Amziane, M. Sonebi, Overview on biobased building material made with plant aggregate, *RILEM Tech. Lett.* 1 (2016) 31–38. https://doi.org/10.21809/rilemtechlett.2016.9.

[38] E. Parcesepe, R.F. De Masi, C. Lima, G.M. Mauro, M.R. Pecce, G. Maddaloni, Assessment of mechanical and thermal properties of hemp-lime mortar, *Materials* 14 (2021) 882. https://doi.org/10.3390/ma14040882.

[39] F. Pacheco-Torgal, S. Jalali, Cementitious building materials reinforced with vegetable fibres: A review, *Constr. Build. Mater.* 25 (2011) 575–581. https://doi.org/10.1016/j.conbuildmat.2010.07.024.

[40] O. Onuaguluchi, N. Banthia, Plant-based natural fibre reinforced cement composites: A review, *Cem. Concr. Compos.* 68 (2016) 96–108. https://doi.org/10.1016/j.cemconcomp.2016.02.014.

[41] J. Wei, C. Meyer, Degradation mechanisms of natural fiber in the matrix of cement composites, *Cem. Concr. Res.* 73 (2015) 1–16. https://doi.org/10.1016/j.cemconres.2015.02.019.

[42] D. Sedan, C. Pagnoux, A. Smith, T. Chotard, Mechanical properties of hemp fibre reinforced cement: Influence of the fibre/matrix interaction, *J. Eur. Ceram. Soc.* 28 (2008) 183–192. https://doi.org/10.1016/j.jeurceramsoc.2007.05.019.

[43] J. Claramunt, M. Ardanuy, J.A. García-Hortal, R.D. Tolêdo Filho, The hornification of vegetable fibers to improve the durability of cement mortar composites, *Cem. Concr. Compos.* 33 (2011) 586–595. https://doi.org/10.1016/j.cemconcomp.2011.03.003.

[44] N. Ranjbar, M. Zhang, Fiber-reinforced geopolymer composites: A review, *Cem. Concr. Compos.* 107 (2020) 103498. https://doi.org/10.1016/j.cemconcomp.2019.103498.

[45] G. Silva, S. Kim, R. Aguilar, J. Nakamatsu, Natural fibers as reinforcement additives for geopolymers – A review of potential eco-friendly applications to the construction industry, *Sustain. Mater. Technol.* 23 (2020) e00132. https://doi.org/10.1016/j.susmat.2019.e00132.

[46] I. Schwarzová, N. Stevulová, T. Melichar, Lightweight composites based on technical hemp hurds in construction industry, *Chem. Eng. Trans.* 57 (2017) 1369–1374. https://doi.org/10.3303/CET1757229.

[47] X. Li, L.G. Tabil, S. Panigrahi, Chemical treatments of natural fiber for use in natural fiber-reinforced composites: A review, *J. Polym. Environ.* 15 (2007) 25–33. https://doi.org/10.1007/s10924-006-0042-3.

[48] M.M. Kabir, H. Wang, K.T. Lau, F. Cardona, Chemical treatments on plant-based natural fibre reinforced polymer composites: An overview, *Compos. Part B Eng.* 43 (2012) 2883–2892. https://doi.org/10.1016/j.compositesb.2012.04.053.

[49] Y. Xie, C.A.S. Hill, Z. Xiao, H. Militz, C. Mai, Silane coupling agents used for natural fiber/polymer composites: A review, *Compos. Part A Appl. Sci. Manuf.* 41 (2010) 806–819. https://doi.org/10.1016/j.compositesa.2010.03.005.

[50] M. Abdelmouleh, S. Boufi, A. Ben Salah, M.N. Belgacem, A. Gandini, Interaction of silane coupling agents with cellulose, *Langmuir* 18 (2002) 3203–3208. https://doi.org/10.1021/la011657r.

[51] M. Abdelmouleh, S. Boufi, M.N. Belgacem, A. Dufresne, Short natural-fibre reinforced polyethylene and natural rubber composites: Effect of silane coupling agents and fibres loading, *Compos. Sci. Technol.* 67 (2007) 1627–1639. https://doi.org/10.1016/j.compscitech.2006.07.003.

[52] D. Klemm, F. Kramer, S. Moritz, T. Lindström, M. Ankerfors, D. Gray, A. Dorris, Nanocelluloses: A new family of nature-based materials, *Angew. Chem. Int. Ed.* 50 (2011) 5438–5466. https://doi.org/10.1002/anie.201001273.

[53] R.J. Moon, A. Martini, J. Nairn, J. Simonsen, J. Youngblood, Cellulose nanomaterials review: structure, properties and nanocomposites, *Chem. Soc. Rev.* 40 (2011) 3941–3994. https://doi.org/10.1039/C0CS00108B.

[54] Y. Habibi, L.A. Lucia, O.J. Rojas, Cellulose nanocrystals: Chemistry, self-assembly, and applications, *Chem. Rev.* 110 (2010) 3479–3500. https://doi.org/10.1021/cr900339w.

[55] A. Dufresne, Nanocellulose: a new ageless bionanomaterial, *Mater. Today* 16 (2013) 220–227. https://doi.org/10.1016/j.mattod.2013.06.004.

[56] K.-Y. Lee, Y. Aitomäki, L.A. Berglund, K. Oksman, A. Bismarck, On the use of nanocellulose as reinforcement in polymer matrix composites, *Compos. Sci. Technol.* 105 (2014) 15–27. https://doi.org/10.1016/j.compscitech.2014.08.032.

[57] Y. Cao, P. Zavattieri, J. Youngblood, R. Moon, J. Weiss, The influence of cellulose nanocrystal additions on the performance of cement paste, *Cem. Concr. Compos.* 56 (2015) 73–83. https://doi.org/10.1016/j.cemconcomp.2014.11.008.

[58] T. Fu, F. Montes, P. Suraneni, J. Youngblood, J. Weiss, The influence of cellulose nanocrystals on the hydration and flexural strength of Portland cement pastes, *Polymers* 9 (2017) 424. https://doi.org/10.3390/polym9090424.

[59] R. Roopchund, J. Andrew, B. Sithole, Using cellulose nanocrystals to improve the mechanical properties of fly ash-based geopolymer construction materials, *Eng. Sci. Technol. Int. J.* 25 (2022) 100989. https://doi.org/10.1016/j.jestch.2021.04.008.

[60] K. Ramamurthy, E.K. Kunhanandan Nambiar, G. Indu Siva Ranjani, A classification of studies on properties of foam concrete, *Cem. Concr. Compos.* 31 (2009) 388–396. https://doi.org/10.1016/j.cemconcomp.2009.04.006.

[61] F. Asdrubali, F. D'Alessandro, S. Schiavoni, A review of unconventional sustainable building insulation materials, *Sustain. Mater. Technol.* 4 (2015) 1–17. https://doi.org/10.1016/j.susmat.2015.05.002.

[62] ASTM C618-23, Standard Specification for Coal Fly Ash and Raw or Calcined Natural Pozzolan for Use in Concrete, ASTM International, West Conshohocken, PA, 2023.

[63] D. Bondeson, A. Mathew, K. Oksman, Optimization of the isolation of nanocrystals from microcrystalline cellulose by acid hydrolysis, *Cellulose* 13 (2006) 171–180. https://doi.org/10.1007/s10570-006-9061-4.

[64] ASTM C109/C109M-21, Standard Test Method for Compressive Strength of Hydraulic Cement Mortars (Using 2-in. or [50-mm] Cube Specimens), ASTM International, West Conshohocken, PA, 2021.

[65] ASTM C177-19, Standard Test Method for Steady-State Heat Flux Measurements and Thermal Transmission Properties by Means of the Guarded-Hot-Plate Apparatus, ASTM International, West Conshohocken, PA, 2019.

[66] ASTM C666/C666M-15, Standard Test Method for Resistance of Concrete to Rapid Freezing and Thawing, ASTM International, West Conshohocken, PA, 2015.

[67] C. Rode, R.H. Peuhkuri, L.H. Mortensen, K.K. Hansen, B. Time, A. Gustavsen, T. Ojanen, J. Ahonen, K. Svennberg, J. Arfvidsson, Moisture buffering of building materials, Report BYG·DTU R-126, Technical University of Denmark, Kongens Lyngby, 2005.

[68] ISO 14040:2006, Environmental management – Life cycle assessment – Principles and framework, International Organization for Standardization, Geneva, 2006.

[69] ISO 14044:2006, Environmental management – Life cycle assessment – Requirements and guidelines, International Organization for Standardization, Geneva, 2006.

[70] T.C. Powers, A working hypothesis for further studies of frost resistance of concrete, *J. Am. Concr. Inst.* 41 (1945) 245–272.

[71] G.W. Scherer, Crystallization in pores, *Cem. Concr. Res.* 29 (1999) 1347–1358. https://doi.org/10.1016/S0008-8846(99)00002-2.